PHYSICAL REVIEW B **95**, 220403(R) (2017)

Manganese-induced magnetic symmetry breaking and its correlation with the metal-insulator transition in bilayered $Sr_3(Ru_{1-x}Mn_x)_2O_7$

Qiang Zhang,[1,2] Feng Ye,[2] Wei Tian,[2] Huibo Cao,[2] Songxue Chi,[2] Biao Hu,[1] Zhenyu Diao,[1]
David A. Tennant,[2] Rongying Jin,[1] Jiandi Zhang,[1] and Ward Plummer[1]
[1]*Department of Physics and Astronomy, Louisiana State University, Baton Rouge, Louisiana 70803, USA*
[2]*Oak Ridge National Laboratory, Oak Ridge, Tennessee 37831, USA*

(Received 30 December 2016; revised manuscript received 22 March 2017; published 12 June 2017)

Bilayered $Sr_3Ru_2O_7$ is an unusual metamagnetic metal with inherently antiferromagnetic (AFM) and ferromagnetic (FM) fluctuations. Partial substitution of Ru by Mn results in the establishment of a metal-insulator transition (MIT) at T_{MIT} and AFM ordering at T_{M} in $Sr_3(Ru_{1-x}Mn_x)_2O_7$. Using elastic neutron scattering, we investigated the effect of Mn doping on the magnetic structure, in-plane magnetic correlation lengths and their correlation to the MIT in $Sr_3(Ru_{1-x}Mn_x)_2O_7$ ($x = 0.06$ and 0.12). With the increase of Mn doping (x) from 0.06 to 0.12 or the decrease of temperatures for $x = 0.12$, an evolution from an in-plane short-range to long-range antiferromagnetic (AFM) ground state occurs. For both compounds, the magnetic ordering has a double-stripe configuration, and the onset of magnetic correlation with an anisotropic behavior coincides with the sharp rise in electrical resistivity and specific heat. Since it does not induce a measurable lattice distortion, the double-stripe antiferromagnetic order with anisotropic spin texture breaks symmetry from a C_{4v} crystal lattice to a C_{2v} magnetic sublattice. These observations shed light on an age-old question regarding the Slater versus Mott-type MIT.

DOI: 10.1103/PhysRevB.95.220403

Bilayered ruthenate $Sr_3Ru_2O_7$ and its derivatives have attracted considerable attention due to their intriguing physical properties resulting from the interplay between charge, spin, orbital, and lattice degrees of freedom. The undoped $Sr_3Ru_2O_7$ [Fig. 1(a)] is a paramagnetic metal with the electrical conduction in the RuO_2 layers [1] and no long-range magnetic order, although magnetic susceptibility exhibits a peak at ∼18 K [2]. Instead, $Sr_3Ru_2O_7$ shows two-dimensional (2D) ferromagnetic (FM) fluctuations above 18 K but incommensurate antiferromagnetic (AFM) fluctuations below 18 K [3]. The competing FM and AFM interactions lead to a metamagnetic transition at low temperatures, accompanied with quantum critical behavior at the transition field $H_c \sim 8\,\mathrm{T}\,[H \parallel c$, c defined in Fig. 1(a)] [4–8]. In the vicinity of H_c, there is a very strong increase of electrical resistivity with large anisotropy [9], lattice distortion [10], and spin-density-wave (SDW) phase with a propagation vector $\boldsymbol{q} = (0.233\ 0\ 0)$ along the Ru-O-Ru bond direction [11]. These observations indicate that fourfold rotation symmetry (C_4) is reduced to twofold (C_2), giving rise to a so-called electronic nematic fluid below $T_{\mathrm{nem}} \approx 1\,\mathrm{K}$ [9–15]. In addition to the magnetic field, the electrical resistivity of the anomalous phase strongly responds to other external forces, such as in-plane uniaxial stain [16]. An intriguing question is, would an internal pressure induced by ion substitution also break the symmetry?

With the substitution of $4d$ Ru using more localized $3d$ Mn, the resultant $Sr_3(Ru_{1-x}Mn_x)_2O_7$ reveals drastically different electronic and magnetic properties from the undoped compound [17–20]. With $x > 0.06$, $Sr_3(Ru_{1-x}Mn_x)_2O_7$ exhibits a metal-insulator transition at T_{MIT} (the electrical resistivity slope changes sign) and antiferromagnetic (AFM) magnetic ordering at T_{M} [17,18,20], where T_{M} is determined from the peak in the magnetic susceptibility. Using x-ray absorption spectroscopy and resonant elastic x-ray scattering, Hossain *et al.* [20] investigated the nature of the MIT in $Sr_3(Ru_{1-x}Mn_x)_2O_7$ and concluded that the MIT is of a Mott (electronic correlations) rather than of a Slater (AFM ordering) type. While T_{MIT} increases with increasing x, T_{M} reaches its maximum at $x \sim 0.16$, where the RuO_6 rotation angle approaches zero [17]. The magnetic structure of $Sr_3(Ru_{1-x}Mn_x)_2O_7$ ($x = 0.16$) with the highest T_{M} of 81 K has been determined to be the so-called "E-type" AFM ordering [21], as shown in Fig. 1(c). The moments form long-range order in the ab plane with a short magnetic correlation length along the c axis (5–6 Å), reflecting a quasi-two-dimensional (2D) character. The in-plane spin arrangements are "up-up-down-down" along the sides and antiparallel/parallel along the diagonal direction of the (Ru/Mn)-(Ru/Mn) square lattice. Such a magnetic configuration is surprising in the context of a square lattice structure. Emergent phenomena induced by Mn doping raises a few interesting questions: (1) How does the magnetic correlation length evolve with Mn doping, starting with fluctuations in the parent compound? (2) How can an E-type magnetic order form in a square lattice? (3) What is the relationship between the MIT and the magnetic transition? Using elastic neutron scattering, we show that substituting Mn for Ru in $Sr_3(Ru_{1-x}Mn_x)_2O_7$ stabilizes the long-range AFM order with a double-stripe magnetic structure in the ab plane (C_{2v}), while the crystal lattice retains C_{4v} symmetry. For the three Mn concentrations studied ($x = 0.06$, 0.12, 0.16), the onset of magnetic correlation coincides with a sharp rise in electrical resistivity, indicating a Slater-like MIT transition [22], that is, a MIT due to the formation of magnetic ordering. These features and the anisotropy in the magnetic correlation lengths set $Sr_3(Ru_{1-x}Mn_x)_2O_7$ as a unique magnetic system, indicative of a magnetic crystal.

The $Sr_3(Ru_{1-x}Mn_x)_2O_7$ ($x = 0.06$ and 0.12) (denoted as SRMO6 and SRMO12 hereafter) crystals were grown using the floating-zone technique, and were well characterized [17]. Figure 1(b) shows the temperature dependence of the in-plane magnetic susceptibility (χ_{ab}) for SRMO6 and SRMO12. For comparison, χ_{ab} for $x = 0.16$ is also presented. Aligned SRMO6 and SRMO12 single crystals were used for the elastic neutron diffraction at the fixed-incident-energy (wavelength

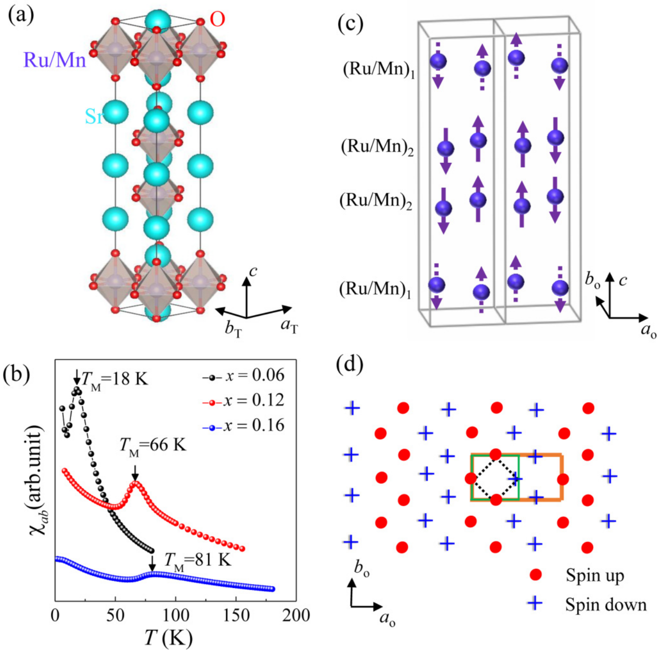

FIG. 1. (a) A 3D view of the tetragonal unit cell for $Sr_3(Ru_{1-x}Mn_x)_2O_7$. (b) Temperature dependence of the in-plane magnetic susceptibility χ_{ab} for $Sr_3(Ru_{1-x}Mn_x)_2O_7$ ($x = 0.06$, 0.12, and 0.16) measured by applying a 1000 Oe magnetic field parallel to the a_ob_o plane. (c) The schematic magnetic structure of $Sr_3(Ru_{1-x}Mn_x)_2O_7$ ($x = 0.06$ and 0.12) obtained from the refinement of our neutron diffraction data at 4 K, where a_o and b_o are the axes of the orthorhombic unit cell. (d) The in-plane double-stripe AFM spin structure of $Sr_3(Ru_{1-x}Mn_x)_2O_7$. The solid green square shows the orthorhombic unit cell with Ru/Mn atoms at the center of each edge. The black dotted square indicates the tetragonal unit cell with Ru/Mn atoms at the corners. The orange rectangle shows the (2×1) magnetic unit cell.

$\lambda = 2.365$ Å) triple-axis spectrometer HB1A and four-circle single-crystal diffractometer HB3A with a wavelength of 1.542 Å (which includes ~1.4% $\lambda/2$ contamination) at the High Flux Isotope Reactor (HFIR) at Oak Ridge National Laboratory, USA.

Similar to undoped $Sr_3Ru_2O_7$ [23,24], the structure of $Sr_3(Ru_{1-x}Mn_x)_2O_7$ ($x = 0.06$, 0.12, and 0.16) at room temperature (RT) is orthorhombic with space group *Bbcb*. The orthorhombicity results from octahedral rotation, thus yielding the same in-plane lattice constants (i.e., $a_o = b_o$). Figure 1(a) shows a tetragonal unit cell for $Sr_3(Ru_{1-x}Mn_x)_2O_7$ where (Ru/Mn) ions form a square lattice with (Ru/Mn)-O-(Ru/Mn) bond directions pointing along the tetragonal crystalline axes (a_T and b_T). Due to octahedral rotation, the real unit cell is orthorhombic with $a_o = b_o = \sqrt{2}a_T$, as marked by the green square in Fig. 1(d). The *E*-type magnetic unit cell is a (2×1) supercell, represented by the orange rectangle in Fig. 1(d). Within the neutron resolution in HB3A, no difference between the lattice parameters a_o and b_o is observed for SRMO6 and SRMO12 between RT and 5 K. The lattice constants are $a_o = b_o = 5.4885(4)$ Å, $c = 20.5277(6)$ Å for SRMO12 and $a_o = b_o = 5.4711(3)$ Å, $c = 20.7146(5)$ for SRMO6 at 5 K, with a 0.2% change in volume.

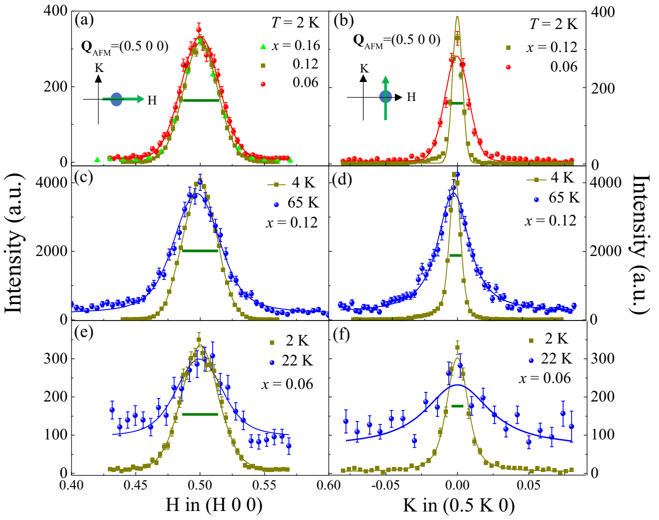

FIG. 2. (a) Longitudinal *H* scans along the a_o axis for $x = 0.06$, 0.12, and 0.16 at 2 K. (b) Transverse *K* scans along the b_o axis for $x = 0.06$ and 0.12 at 2 K. The solid curves are fits to the data using the Gaussian function to compare the FWHM among different compounds at 2 K. The longitudinal *H* scans and transverse *K* scans are illustrated by green arrows in the insets of (a) and (b), respectively. (c) Longitudinal *H* scans along the a_o axis, and (d) transverse *K* scans along the b_o axis through $\mathbf{Q}_{AFM} = (0.5\ 0\ 0)$ at 4 K (below T_M) and 65 K (~T_M) for $x = 0.12$. (e) Longitudinal *H* scans along the a_o axis, and (f) transverse *K* scans along the b_o axis through $\mathbf{Q}_{AFM} = (0.5\ 0\ 0)$ at 2 K (below T_M) and 22 K (>T_M) for $x = 0.06$. The solid lines in (c)–(f) are the fits to the data using our model to obtain the intrinsic magnetic correlation length as described in the main text. The instrumental resolution is shown as the horizontal bars.

Figures 2(a) and 2(b) show, at 2 K, the longitudinal *H* scan along the a_o axis for SRMO6, SRMO12, and SRMO16 ($x = 0.16$), and the transverse *K* scan along the b_o axis for SRMO6 and SRMO12 through the AFM propagation vector $\mathbf{Q}_{AFM} = (0.5\ 0\ 0)$, respectively. The longitudinal *H* scans for SRMO12 and SRMO16 overlap each other and are resolution limited, indicating that the $x = 0.12$ compound behaves similarly to $x = 0.16$ with in-plane long-range AFM order at low temperatures. However, both the longitudinal and transverse scans for SRMO6 at 2 K are broader than those of SRMO12. The broader magnetic peaks seen in SRMO6 cannot be related to the differences in the sample quality/crystallinity, since it has a mosaic similar to that of SRMO12. We thus conclude the broader peaks are a reflection of intrinsic magnetism, which indicates SRMO6 forms only short-range but not long-range AFM order in the *ab* plane at 2 K.

Magnetic structure refinement on $Sr_3(Ru_{1-x}Mn_x)_2O_7$ ($x = 0.06$ and 0.12) at 5 K reveals a double-stripe AFM order with the following features: (1) The ordered moment on the $(Ru/Mn)_1$ and $(Ru/Mn)_2$ sites is the same and points along the *c* axis [see Fig. 1(c)]. (2) In the *ab* plane, spins form two interpenetrating stripelike AFM orderings with double ferromagnetic stripes along the b_o direction, alternating antiferromagnetically along the a_o direction [see Fig. 1(d)]. (3) The spin texture is the same for both layers within the unit cell [see Fig. 1(c)]. As *x* reduces from 0.16 to 0.06, the spin configuration at 5 K remains similar but there is a crossover

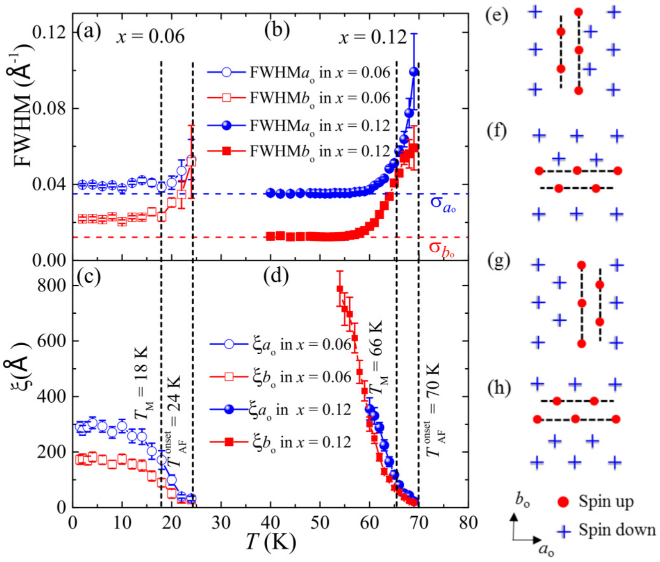

FIG. 3. Temperature dependence of the FWHM along the a_o and b_o axes for (a) $x = 0.06$ and (b) $x = 0.12$ obtained from fits to the data using the Gaussian function. The horizontal dashed blue and red lines indicate the instrumental resolution σ_{a_o} and σ_{b_o}, respectively. (c) and (d) show the temperature dependence of the magnetic correlation length ξ_{a_o} and ξ_{b_o} for $x = 0.06$ and $x = 0.12$, respectively. (e)–(h) Four degenerate magnetic states of the double-stripe AFM order in $Sr_3(Ru_{1-x}Mn_x)_2O_7$. The two dashed lines indicate the directions of the double ferromagnetic stripes.

from the long-range to the short-range order. Furthermore, the ordered moment of Ru/Mn becomes smaller, from $0.51\mu_B$ for SRMO12, to $0.18\mu_B$ for SRMO6.

The temperature (T) dependence of the longitudinal H (along the a_o direction) and transverse K scans (along the b_o direction) through $\mathbf{Q}_{AFM}$ in SRMO6 and SRMO12 is measured. Figures 2(c) and 2(d) show these scans at $T = 4$ and 65 K for SRMO12. While both H and K scans are resolution limited at 4 K, the peak is clearly broadened at 65 K, consistent with the resonant x-ray scattering results [20], which provides direct evidence of the short-range order above ≈60 K. A similar trend is also observed in SRMO6, as presented in Figs. 2(e) and 2(f), which show the H and K scans at $T = 2$ and 22 K. Note the broadening is also seen above ≈18 K, indicating that the short-range order in SRMO6 extends above T_M. The magnetic peaks eventually disappear at ∼24 K for SRMO6 and ∼70 K for SRMO12 when T approaches T_{MIT}, which is ∼24 K for SRMO6 and ∼90 K for SRMO12 [17]. Figures 3(a) and 3(b) show the temperature dependence of the full width at half maximum (FWHM) for both longitudinal H scans along the a_o axis and transverse K scans along the b_o axis obtained from the fits to the data using the Gaussian function for SRMO6 and SRMO12, respectively. The short-range order with relatively high FWHM starts to be detected at $T_{AF}^{onset} > T_M$. As T decreases, FWHM decreases gradually and appears to be saturated at around 18 and 60 K for SRMO6 and SRMO12, respectively.

In order to determine the intrinsic correlation lengths along the a_o and b_o directions, we fit the experimental line shape of the longitudinal and transverse scans to a Lorentz function $L(q) = \frac{c}{1+(q\xi)^2}$, convoluted with the instrumental resolution Gaussian function $G(q) = \exp\left(-q^2/\left[2\left(\frac{\sigma}{2\sqrt{\ln 4}}\right)^2\right]\right)$ [25]. Here, ξ (ξ^{-1} is the half width at half maximum of the Lorentzian function) is defined as the magnetic correlation length [26], and σ is the FWHM of an instrumental resolution Gaussian function with $\sigma_{a_o} \approx 0.0353\ \text{Å}^{-1}$ and $\sigma_{b_o} \approx 0.0127\ \text{Å}^{-1}$ [see the two horizontal dashed lines in Figs. 3(a) and 3(b)] determined by the RESLIB program [27]. The deconvolution yields the magnetic correlation lengths ξ_{a_o} and ξ_{b_o} plotted in Figs. 3(c) and 3(d). The onset for short-range magnetic order is marked using T_{AF}^{onset} for both SRMO6 and SRMO12. As the temperature is lowered, both ξ_{a_o} and ξ_{b_o} increase with anisotropic behavior ($\xi_{a_o} > \xi_{b_o}$). Below T_M, the magnetic correlation saturates for SRMO06 with $\xi_{a_o} \sim 1.5\xi_{b_o}$, confirming the short-range order. The data for SRMO12 also show anisotropic behavior below T_{AF}^{onset}, with $\xi_{a_o} > \xi_{b_o}$. True long-range magnetic order is evident in ξ_{b_o} below ≈60 K ($<T_M$). Unfortunately, we cannot determine ξ_{a_o} below ≈60 K because the error bar becomes too large. It should be noted that the anisotropic behavior observed in both compositions is counterintuitive, since the spin structure breaks the crystal symmetry [Fig. 1(c)]. One would expect that the lattice would try to destroy the magnetic crystallization.

It would be of importance to address the magnetic interactions and the origin of the anisotropic magnetic correlation length in the double-stripe order in $Sr_3(Ru_{1-x}Mn_x)_2O_7$. To stabilize each of the two stripes, AFM next-nearest-neighbor (NNN) coupling should be larger than half of the AFM nearest-neighbor (NN) couplings within each stripe ordered sublattice, as reported in Fe-based pnictides with a single-stripe order [28] and FeTe with a double-stripe order [29]. Since the NN and NNN intracouplings within each stripe ordered sublattice are AFM couplings, the NN bonds along the spin-parallel (b_o) direction are frustrated as compared to the NN bonds along the spin-antiparallel (a_o) direction, resulting in $\xi_{a_o} > \xi_{b_o}$. Interestingly, unlike the single-stripe order case with two degenerate magnetic stripe states (π,0) and (0,π) [26,28], the double-stripe AFM order in $Sr_3(Ru_{1-x}Mn_x)_2O_7$ has four degenerate magnetic stripe states with spin frustration, as depicted in Figs. 3(e)–3(h).

Figure 4(a) shows the temperature dependence of the integrated intensities for the magnetic peak (0.5 0 0) for three different Mn concentrations ($x = 0.06$, 0.12, and 0.16). Note that the onset of magnetic order occurs prior to T_M, i.e., $T_{AF}^{onset} > T_M$. Interestingly, for every Mn concentration studied, there is a dramatic increase in the resistivity (T_ρ^{rise}), much more pronounced than that at T_{MIT}. This is clearly demonstrated in the inset of Fig. 4(a): At the onset of the specific heat anomaly (the same as T_{AF}^{onset}), there is a sharp rise in the resistivity, i.e., $T_{AF}^{onset} = T_\rho^{rise}$. Figure 4(b) summarizes the temperature and Mn-content (x) dependence of the magnetism. Regions I and II denote the paramagnetic metallic (PM-M) and paramagnetic insulating (defined by $d\rho/dT < 0$) state, respectively. Region III is the short-range double-stripe ordered insulating state (SR-I), and region IV is the long-range double-stripe ordered insulating state (LR-I). The magnetic structure in region III is schematically shown in the inset of Fig. 4(b). We emphasize three important results in our phase diagram. First, there is anisotropy in the magnetic correlation length, i.e., $\xi_{a_o} > \xi_{b_o}$ in region III, which is related to the anisotropic spin texture.

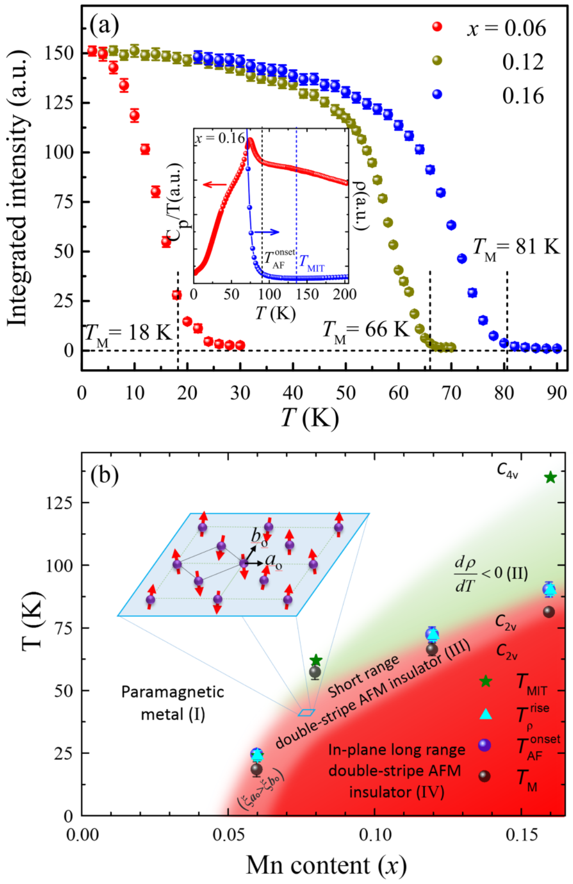

FIG. 4. (a) Temperature dependence of the integrated intensities of a (0.5 0 0) magnetic peak obtained from fits to their longitudinal scans along the a_o axis using the Gaussian function for $x = 0.06, 0.12,$ and 0.16. The inset shows the temperature dependence of specific heat plotted as C_p/T and resistivity for $x = 0.16$, demonstrating a sharp resistivity rise at the onset of the specific heat anomaly and magnetic correlation. (b) Phase diagram of $Sr_3(Ru_{1-x}Mn_x)_2O_7$ constructed by combining elastic neutron scattering results with previously published data [17]: Region I is the paramagnetic metallic state, region II is the paramagnetic insulating state defined by $d\rho/dT < 0$, region III is the short-range double-stripe AFM insulating state, and region IV is the long-range double-stripe AFM insulating state. The inset is the short-range double-stripe AFM structure in region III where the anisotropic magnetic correlation lengths with $\xi_{a_o} > \xi_{b_o}$ exist.

Second, the short-range double-stripe AFM order (region III) becomes detectable below T_{AF}^{onset} ($>T_M$), and although the splitting between T_{MIT} and T_{AF}^{onset} becomes more pronounced as x increases from 0.06 to 0.16, a huge resistivity response always accompanies the onset of magnetic correlation at T_{AF}^{onset}, indicating that $Sr_3(Ru_{1-x}Mn_x)_2O_7$ ($0.06 \ll x \leqslant 0.16$) is a Slater-like insulator. The long-range magnetic order develops upon cooling, as reflected by the enhanced magnetic correlation lengths (region IV). Third, given that there is no structure change across T_{MIT} and T_M within the neutron resolution, $Sr_3(Ru_{1-x}Mn_x)_2O_7$ ($x = 0.06, 0.12, 0.16$) should have the same structural symmetry as the undoped sample [3], with fourfold symmetry (C_{4v}) in the ab plane [17]. The double-stripe magnetic structure below T_{AF}^{onset} has twofold symmetry (C_{2v}) due to the anisotropic spin texture.

To understand our experimental results, we compare the Mn-induced magnetism with that induced by a magnetic field. Mn doping induces a double-stripe AFM order with a propagation vector (0.5 0 0) along the diagonal direction of a (Ru/Mn)-(Ru/Mn) square lattice. In contrast, a magnetic field induces SDW with a propagation vector (0.233 0.233 0) and resistivity anisotropy due to the nematic order along the side of the Ru-Ru square lattice of $Sr_3Ru_2O_7$ [11]. In spite of these differences, both Mn doping and a magnetic field result in a reduced symmetry in the physical properties. In the case of $Sr_3(Ru_{1-x}Mn_x)_2O_7$, the symmetry breaking occurs below T_{AF}^{onset}. If the nematic order emerges below $T_{nem}(= T_{AF}^{onset})$ in region III, it could act as a coupling to lock the nearest-neighbor spins within the individual stripe ordered sublattices in a ferromagnetic- or antiferromagneticlike configuration [28,30], and therefore the frustration resulting from four degenerate magnetic stripe states present at higher temperatures can be lifted, leading to symmetry breaking below T_{AF}^{onset}.

In summary, we have investigated Mn-induced magnetism through elastic neutron scattering in bilayered $Sr_3(Ru_{1-x}Mn_x)_2O_7$. With increasing Mn concentration, the AFM interaction gradually increases, initially forming a short-range double-stripe AFM order and then long-range order in the ab plane. For both $x = 0.06$ and 0.12, the magnetic correlation becomes detectable at $T_{AF}^{onset} > T_M$. The double-stripe AFM configuration presents C_{2v} symmetry below T_{AF}^{onset}, which is lower than the crystal symmetry (C_{4v}). An anisotropic magnetic correlation length with $\xi_{a_o} > \xi_{b_o}$ is found in the short-range double-stripe AFM order, which results from the frustrated nearest-neighbor bonds along the direction of the ferromagnetic stripes. The symmetry breaking may reflect a complex yet interesting underlying physics, such as magnetic crystal formation.

The measurement of magnetic correlation enables us to understand the interplay between magnetism, symmetry breaking, and MIT in $Sr_3(Ru_{1-x}Mn_x)_2O_7$. Due to an inherent magnetic instability in $Sr_3Ru_2O_7$, the introduction of magnetic Mn with a narrower 3d band (compared to Ru) stabilizes the AFM interaction and results in both magnetic and MIT transitions. With a low Mn concentration, we observe that the magnetic correlation becomes measurable at MIT, indicating Slater-like spin-charge coupling. While the MIT occurs at temperatures higher than the magnetic correlation temperature as x increases to ~0.16, there is always a sharp resistivity rise, and a specific heat anomaly at the onset of magnetic order, indicating that the transition is driven by spin instead of charge correlation or a structural change. The separation between the MIT and the true magnetic transition suggests that the electron-electron interaction continuously increases with further increasing x (>0.16), and this might eventually drive the system to a Mott-type insulator, which requires the investigation in the further.

We would like to thank Mohammad Saghayezhian with his assistance using the Voight function in ORIGINLAB software to fit the data and Dalgis Mesa for sharing with us unpublished data from her thesis. Primary support for this study came from the U.S. Department of Energy under EPSCoR Grant No. DE-SC0012432, with additional support from the Louisiana Board of Regents. Use of the high flux isotope reactor at Oak Ridge National Laboratory was supported by the U.S. Department of Energy, Office of Basic Energy Sciences, Scientific User Facilities Division.

[1] G. Cao, S. McCall, and J. E. Crow, Phys. Rev. B **55**, R672(R) (1997); A. Tamai, M. P. Allan, J. F. Mercure, W. Meevasana, R. Dunkel, D. H. Lu, R. S. Perry, A. P. Mackenzie, D. J. Singh, Z.-X. Shen, and F. Baumberger, Phys. Rev. Lett. **101**, 026407 (2008); Y. Liu, R. Jin, Z. Q. Mao, K. D. Nelson, M. K. Haas, and R. J. Cava, Phys. Rev. B **63**, 174435 (2001).

[2] Q. Huang, J. W. Lynn, R. W. Erwin, J. Jarupatrakorn, and R. J. Cava, Phys. Rev. B **58**, 8515 (1998).

[3] L. Capogna, E. M. Forgan, S. M. Hayden, A. Wildes, J. A. Duffy, A. P. Mackenzie, R. S. Perry, S. Ikeda, Y. Maeno, and S. P. Brown, Phys. Rev. B **67**, 012504 (2003).

[4] S. I. Ikeda, Y. Maeno, S. Nakatsuji, M. Kosaka, and Y. Uwatoko, Phys. Rev. B **62**, R6089 (2000).

[5] R. S. Perry, L. M. Galvin, S. A. Grigera, L. Capogna, A. J. Schofield, A. P. Mackenzie, M. Chiao, S. R. Julian, S. I. Ikeda, S. Nakatsuji, Y. Maeno, and C. Pfleiderer, Phys. Rev. Lett. **86**, 2661 (2001).

[6] S. A. Grigera, R. S. Perry, A. J. Schofield, M. Chiao, S. R. Julian, G. G. Lonzarich, S. I. Ikeda, Y. Maeno, A. J. Millis, and A. P. Mackenzie, Science **294**, 329 (2001).

[7] A. W. Rost, R. S. Perry, J.-F. Mercure, A. P. Mackenzie, and S. A. Grigera, Science **325**, 1360 (2009).

[8] C. Pfleiderer, S. R. Julian, and G. G. Lonzarich, Nature (London) **414**, 427 (2001).

[9] R. A. Borzi, S. A. Grigera, J. Farrell, R. S. Perry, S. J. S. Lister, S. L. Lee, D. A. Tennant, Y. Maeno, and A. P. Mackenzi, Science **315**, 214 (2007).

[10] C. Stingl, R. S. Perry, Y. Maeno, and P. Gegenwart, Phys. Rev. Lett. **107**, 026404 (2011).

[11] C. Lester, S. Ramos, R. S. Perry, T. P. Croft, R. I. Bewley, T. Guidi, P. Manuel, D. D. Khalyavin, E. M. Forgan, and S. M. Hayden, Nat. Mater. **14**, 373 (2015).

[12] W.-C. Lee and C. Wu, Phys. Rev. B **80**, 104438 (2009).

[13] M. Tsuchiizu, Y. Ohno, S. Onari, and H. Kontani, Phys. Rev. Lett. **111**, 057003 (2013).

[14] A. W. Rosta, S. A. Grigera, J. A. N. Bruin, R. S. Perry, D. Tian, S. Raghu, S. A. Kivelson, and A. P. Mackenzie, Proc. Natl. Acad. Sci. USA **108**, 16549 (2011).

[15] A. P. Mackenzie, J. A. N. Bruin, R. A. Borzi, A. W. Rost, and S. A. Grigera, Physica C **481**, 207 (2012).

[16] D. Brodsky, M. Barber, J. Bruin, R. Borzi, S. Grigera, R. Perry, A. Mackenzie, and C. Hicks, arXiv:1512.04216.

[17] B. Hu, G. T. McCandless, V. O. Garlea, S. Stadler, Y. Xiong, J. Y. Chan, E. W. Plummer, and R. Jin, Phys. Rev. B **84**, 174411 (2011).

[18] R. Mathieu, A. Asamitsu, Y. Kaneko, J. P. He, X. Z. Yu, R. Kumai, Y. Onose, N. Takeshita, T. Arima, H. Takagi, and Y. Tokura, Phys. Rev. B **72**, 092404 (2005).

[19] G. Li, Q. Li, M. Pan, B. Hu, C. Chen, J. Teng, Z. Diao, J. Zhang, R. Jin, and E. W. Plummer, Sci. Rep. **3**, 2882 (2013).

[20] M. A. Hossain *et al.*, Phys. Rev. B **86**, 041102 (2012); Sci. Rep. **3**, 2299 (2013).

[21] D. Mesa, F. Ye, S. Chi, J. A. Fernandez-Baca, W. Tian, B. Hu, R. Jin, E. W. Plummer, and J. Zhang., Phys. Rev. B **85**, 180410(R) (2012).

[22] J. C. Slater, Phys. Rev. **82**, 538 (1951).

[23] H. Shaked, J. D. Jorgensen, O. Chmaissem, S. Ikeda, and Y. Maeno, J. Solid State Chem. **154**, 361 (2000).

[24] R. Kiyanagi, K. Tsuda, N. Aso, H. Kimura, Y. Noda, Y. Yoshida, S.-I. Ikeda, and Y. Uwatoko, J. Phys. Soc. Jpn. **73**, 639 (2004).

[25] We used both the RESLIB program and the Voigt function in ORIGINLAB to extract the magnetic Lorentzian function from experimental data, given a determined instrument Gaussian function.

[26] C. W. H. M. Vennix, E. Frikkee, P. J. T. Eggenkamp, H. J. M. Swagten, K. Kopinga, and W. J. M. deJonge, Phys. Rev. B **48**, 3770 (1993).

[27] A. Zheludev, www.neutron.ethz.ch/research/resources/reslib. Note that the instrument resolution is appreciably larger for longitudinal scans the scattering plane based on the configurations of the triple axis spectrometer at HB1A.

[28] R. M. Fernandes, A. V. Chubukov and J. Schmalian, Nat. Phys. **10**, 97 (2014); R. M. Fernandes and J. Schmalian, Supercond. Sci. Technol. **25**, 084005 (2012).

[29] F. Ma, W. Ji, J. Hu, Z. Y. Lu, and T. Xiang, Phys. Rev. Lett. **102**, 177003 (2009).

[30] Q. Zhang, R. M. Fernandes, J. Lamsal, J. Yan, S. Chi, G. S. Tucker, D. K. Pratt, J. W. Lynn, R. W. McCallum, P. C. Canfield, T. A. Lograsso, A. I. Goldman, D. Vaknin, and R. J. McQueeney., Phys. Rev. Lett. **114**, 057001 (2015).